Title

T lymphocytes from malignant hyperthermia-susceptible mice display aberrations in intracellular calcium signaling and mitochondrial function.

Authors

Yang, Lukun
Dedkova, Elena N
Allen, Paul D
et al.

Publication Date

2021

DOI

10.1016/j.ceca.2020.102325

Peer reviewed

HHS Public Access

Author manuscript

Cell Calcium. Author manuscript; available in PMC 2022 January 01.

Published in final edited form as:

Cell Calcium. 2021 January ; 93: 102325. doi:10.1016/j.ceca.2020.102325.

T lymphocytes from malignant hyperthermia-susceptible mice display aberrations in intracellular calcium signaling and mitochondrial function.

Lukun Yang[1,2], **Elena N. Dedkova**[3], **Paul D. Allen**[3,4], **M. Saleet Jafri**[5], **Alla F. Fomina**[1]

[1]Department of Physiology and Membrane Biology, University of California, Davis, Davis CA 95616, USA

[2]Department of Anesthesiology, the 5th affiliated Hospital of SUN YAT-SEN University, Zhuhai, China, 519000

[3]Department of Molecular Biosciences, University of California, Davis, Davis CA 95616, USA

[4]MH Unit, St. James's University Hospital, University of Leeds, Leeds LS9 7TF United Kingdom

[5]School of Systems Biology, George Mason University, Fairfax VA 22030, USA

Abstract

Gain-of-function *RyR1*-p.R163C mutation in ryanodine receptors type 1 (RyR1) deregulates Ca^{2+} signaling and mitochondrial function in skeletal muscle and causes malignant hyperthermia in humans and mice under triggering conditions. We investigated whether T lymphocytes from heterozygous *RyR1*-p.R163C knock-in mutant mice (HET T cells) display measurable aberrations in resting cytosolic Ca^{2+} concentration ($[Ca^{2+}]_i$), Ca^{2+} release from the store, store-operated Ca^{2+} entry (SOCE), and mitochondrial inner membrane potential ($\Delta\Psi_m$) compared with T lymphocytes from wild-type mice (WT T cells). We explored whether these variables can be used to distinguish between T cells with normal and altered RyR1 genotype.

HET and WT T cells were isolated from spleen and lymph nodes and activated *in vitro* using phytohemagglutinin P. $[Ca^{2+}]_i$ and $\Delta\Psi_m$ dynamics were examined using Fura 2 and tetramethylrhodamine methyl ester fluorescent dyes, respectively. Activated HET T cells displayed elevated resting $[Ca^{2+}]_i$, diminished responses to Ca^{2+} mobilization with thapsigargin, and decreased rate of $[Ca^{2+}]_i$ elevation in response to SOCE compared with WT T cells. Pretreatment

Corresponding Author: Alla F. Fomina, Ph.D., Department of Physiology and Membrane Biology, University of California, Davis, One Shields Ave., Davis CA 95616, USA, Phone: +1-530-754-4454; affomina@ucdavis.edu.

Author Contributions:

Lukun Yang: Investigation, Methodology; **Elena N. Dedkova:** Investigation, Methodology, Data curation; **Paul D. Allen:** Conceptualization, Writing-Original draft preparation; **M. Saleet Jafri:** Formal analysis, Methodology, Writing- Original draft preparation; **Alla F. Fomina:** Conceptualization, Investigation, Supervision, Data curation, Validation, Writing-Reviewing and Editing.

Declaration of interests

The authors declare that they have no known competing financial interests or personal relationships that could have appeared to influence the work reported in this paper.

of HET T cells with ryanodine or dantrolene sodium reduced disparities in the resting $[Ca^{2+}]_i$ and ability of thapsigargin to mobilize Ca^{2+} between HET and WT T cells. While SOCE elicited dissipation of the $\Delta\Psi_m$ in WT T cells, it produced $\Delta\Psi_m$ hyperpolarization in HET T cells. When used as the classification variable, the amplitude of thapsigargin-induced Ca^{2+} transient showed the best promise in predicting the presence of *RyR1*-p.R163C mutation. Other significant variables identified by machine learning analysis were the ratio of resting cytosolic Ca^{2+} level to the amplitude of thapsigargin-induced Ca^{2+} transient and an integral of changes in $\Delta\Psi_m$ in response to SOCE.

Our study demonstrated that gain-of-function mutation in RyR1 significantly affects Ca^{2+} signaling and mitochondrial fiction in T lymphocytes, which suggests that this mutation may cause altered immune responses in its carrier. Our data link the *RyR1*-p.R163C mutation, which causes inherited skeletal muscle diseases, to deregulation of Ca^{2+} signaling and mitochondrial function in immune T cells and establish proof-of-principle for *in vitro* T cell-based diagnostic assay for hereditary RyR1 hyperfunction.

Graphical Abstract

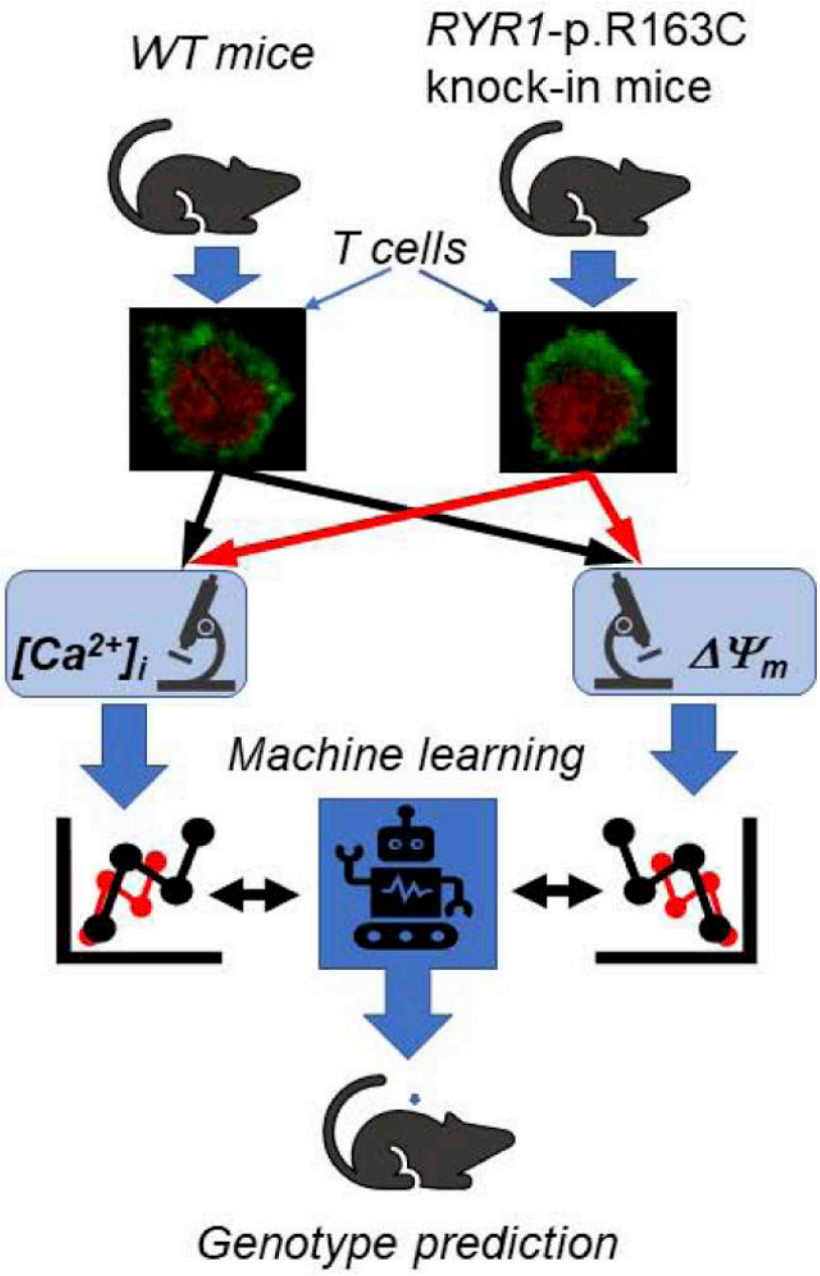

Keywords

T lymphocytes; ryanodine receptor; *RYR1*-p.R163C knock-in mice; intracellular Ca^{2+}; mitochondrial potential; dantrolene sodium

1. INTRODUCTION

Ryanodine receptors (RyR) are a family of intracellular Ca^{2+} release channels located in the membranes of the smooth endoplasmic reticulum. Mutations in the *RYR1* gene causing gain-of-function in RyR type 1 (RyR1) have been associated with several inherited skeletal

muscle diseases, collectively known as *RYR1*-related myopathies, and susceptibility to malignant hyperthermia (MH), a life-threatening condition caused by a massive release of Ca^{2+} via RyR1 from the sarcoplasmic reticulum and subsequent skeletal muscle hypermetabolism [1, 2]. To date, over 700 mutations in the *RYR1* gene, which may be causative for MH and related myopathies, have been identified [3], of which 48 variants were functionally characterized (www.emhg.org). Because there is no obvious correlation between the presence of the specific *RYR1* mutation and severity of the clinical manifestations in patients [2, 4, 5], predicting the susceptibility to MH requires both genetic screening and *in vitro* skeletal muscle functional contracture test, which involves an invasive muscle biopsy [6]. Establishing an easily accessible non-muscle model to study the functional consequences of *RYR1* mutations will enable a more broad exploration of the genotype-phenotype relationship and testing new diagnostic, treatment, or preventive modalities for MH and related myopathies.

Expression of RyR was shown in human and rodent T lymphocytes using the molecular biological, pharmacological, and [^{3}H]-Ryanodine incorporation assays [7–12]. We have shown previously that RyR1 control Ca^{2+} signaling in activated human T cells by regulating Ca^{2+} release from the intracellular store and store-operated Ca^{2+} entry (SOCE) [11, 13]. These findings suggest that inherited impairment in the RyR1 function may cause aberrations in T cell Ca^{2+} signaling. Ca^{2+} released from RyR1 into the narrow space between the endoplasmic reticulum and mitochondria modulates mitochondrial Ca^{2+} uptake, which is driven by a highly negative to the cytosol mitochondrial inner membrane potential ($\Delta\Psi_m$) established by the mitochondrial respiratory chain complexes [14–16]. Mitochondrial Ca^{2+} uptake shapes cytosolic and mitochondrial Ca^{2+} dynamics and regulates multiple mitochondrial processes [17–19]. Thus, it is reasonable to expect that irregularities in Ca^{2+} discharge from the endoplasmic reticulum via RyR1 will affect Ca^{2+} uptake by mitochondria and $\Delta\Psi_m$ in T cells.

In this study, we aimed to determine whether an *RYR1*-p.R163C mutation, one of the most common mutations associated with MH susceptibility in humans [20, 21], alters cytosolic Ca^{2+} signaling and $\Delta\Psi_m$ in T lymphocytes. T cells were collected from a heterozygous knock-in mouse model for the human N-terminal mutation *RYR1*-p.R163C (HET R163C mice) [22]. Out of a total of 15 existing preclinical *RYR1* rodent models, HET R163C mice is one of the few that were extensively studied [23, 24]. HET R163C mice exhibit fulminant MH episodes in response to either volatile anesthetics or environmental heat stress [22] and is one of the three murine models (R163C -RYR1, T4826I-RYR1, and Y522S-RYR1) [22, 25–28], which recapitulate elevated myoplasmic basal free Ca^{2+} concentration ($[Ca^{2+}]_i$) observed in MH-susceptible humans [29, 30] and swine [31]. HET R163C mice exhibit skeletal muscle mitochondrial dysfunction [32], which has been also reported for other RyR1 preclinical murine models (G2435R-RYR1, T4826I-RYR1, and Y522S-RYR1) [33–35]. Thus, HET R163C mice are suitable for this study because they display anomalies in Ca^{2+} signaling and mitochondrial function in skeletal muscle similar to those observed in both MH-susceptible humans and other MH murine models. Here we investigated whether T lymphocytes isolated from the HET R163C mice display measurable aberrations in Ca^{2+} release from the intracellular store, store-operated Ca^{2+} entry (SOCE), and $\Delta\Psi_m$. We explored which of these variables can be used to distinguish between T cells expressing

normal and 'leaky" RyR. Because the essential features of Ca^{2+} signaling are conserved between murine and human T cells [36], we anticipate that results obtained in murine T cells would predict human responses [37].

2. MATERIALS AND METHODS

2.1. Generation and culturing of primary T cells from spleen and lymph nodes of WT and HET R163 mice.

All animal experiments were conducted using protocols approved by the institutional animal care and use committees at the University of California, Davis. Generation and genotyping of *RYR1*-p.R163C mice was performed as previously described [22]. Spleen and lymph nodes were aseptically isolated from adult HET R163C mice and WT littermates of both sexes (45.5 ± 2.1 weeks old; n = 34). The spleen and body weights of mice used in this study are presented in Supplementary Figure 1.

Primary T cells were isolated from WT mice (referred to as WT T cells thereafter) and HET R163C mice (referred to as HET T cells thereafter) using a standard protocol [38] with some modifications. Unless otherwise indicated, all chemicals were from Millipore-Sigma. Briefly, aseptically dissected spleen and lymph nodes were placed into 60-mm cell culture dishes containing ice-cold PBS and minced into small pieces with a razor blade. Tissue pieces were mashed and passed through a 100-μm cell strainer using a 3-ml syringe plunger and ice-cold PBS into a 50-ml conical tube and then centrifuged for 10 min at 200 g at 4 °C. After removing the supernatant, the pellet was resuspended in 5 ml of red blood cell lysis buffer and incubated at 37 °C for 5 min. Red blood cell lysis was stopped with 10 ml of ice-cold cell culture medium supplemented with 10% fetal bovine serum (FBS; Omega Scientific) and cells were then centrifuged for 10 min at 200 g at 4 °C. After removing the supernatant, the pellet was resuspended in a 10 ml cell culture medium, and cells were counted using Bio-Rad TC10 Automated Cell Counter (Bio-Rad Labs). This procedure typically yielded approximately 5×10^7 viable cells per mouse. The CD3+ T cells were purified using the EasySep Mouse T Cell Isolation Kit (Stemcell Technologies) per the manufacturer's instructions. Purified T cells were transferred into cell culture flasks at a density of 0.5×10^6 cells/ml and incubated in RPMI 1640 medium with L-glutamine and HEPES (Gibco-Thermo Fisher Sci), supplemented with 10% FBS, 2% GlutaMAX (Thermo Fisher Sci.), 1% RPMI 1640 vitamin solution, 1% RPMI 1640 amino acid solution, 1% sodium pyruvate, 0.01% β-mercaptoethanol in a 5% CO_2 incubator at 37°C.

2.2. Activation of primary T cells.

A portion of the isolated T cells was incubated overnight in a cell culture medium without stimulation (referred to as resting T cells) and was used for the Ca^{2+} imaging experiments within 24 hours after isolation. Another portion of T cells was activated on the day of isolation with 10 μg/ml phytohemagglutinin P (PHA) [39], which cross-links T cell receptors. Cells from the PHA-treated population are referred to as activated T cells. Viable cells were counted every 24 hours after activation using a hemocytometer. Activated T cells were used for imaging experiments 96–120 hours after activation during the exponential growth phase. Experiments performed on T cells from the same animal on different days

after isolation were considered to be independent. No more than two experiments were performed on cells from the same animal under each experimental condition.

2.3. Intracellular Ca^{2+} imaging.

Estimated $[Ca^{2+}]_i$ values were calculated from Fura-2 Ca^{2+} indicator fluorescence as described previously [13]. Briefly, resting or activated, T cells were plated into a glass-bottomed, 35-mm petri dish (MatTek Life Sci.) coated with 1% w/v polyethyleneimine [40, 41] and loaded with 1 μl/ml Fura-2 AM stock (5 mM in DMSO) and 5 μl/ml of 10% Pluronic F-127 solution in DMSO, in 2 mM Ca^{2+}-containing recording solution. After washing, cells were incubated for an additional 30 min at 37 °C in 2 mM Ca^{2+}-containing recording solution to which either 400 μM ryanodine (Ry; Calbiochem), 50 μM dantrolene sodium (DS; Calbiochem), or vehicle was added. Stock solutions of Ry (10 mM) and DS (10 mM) were prepared in methanol and DMSO, respectively.

A dish with adherent cells was mounted on the stage of a Zeiss Axiovert 200 inverted microscope (Karl Zeiss) equipped with a SenSys CCD camera (Roper Scientific) and a Fura-2 filter set with a wide band emission filter (Chroma Technologies, Rockingham, VT). A Lambda DG-4 filter changer (Sutter Instruments) was used for switching between 340- and 380-nm excitation wavelengths. Fura-2 fluorescence signals evoked by 340- and 380-nm excitation (F_{340} and F_{380}, respectively) were acquired every 12 s. Data acquisition was performed using MetaFluor version 7.0 software (Molecular Devices). Estimated $[Ca^{2+}]_i$ values were calculated from background-subtracted F_{340}/F_{380} ratio values and Fura-2 calibration as previously described [42]. K_d was taken as 248 nM [43]. In each experiment, F_{340} and F_{380} fluorescence signals were acquired from 15–20 cells located in the field of view. The $[Ca^{2+}]_i$ values were calculated for each cell and then averaged for each experiment.

Recording solutions were as follows (in mM): 1) 2 mM Ca^{2+}-containing: 130 mM NaCl, 5.6 mM KCl, 1 mM $MgCl_2$, 2 mM $CaCl_2$, 10 mM Na-Hepes, 10 mM D-glucose; 2) nominally Ca^{2+}-free: 130 mM NaCl, 5.6 mM KCl, 3 mM $MgCl_2$, 1 mM EGTA, 10 mM Na-Hepes, 10 mM D-glucose; 3) nominally Ca^{2+}-free solution supplemented with 1 μM thapsigargin (Tg). The pH of all solutions was 7.3. Solution exchange was performed via a gravity-driven perfusion system that allows for complete solution exchange in the recording chamber within 5 s. Experiments were performed at room temperature in air.

2.4. Mitochondrial Inner Membrane Potential Imaging.

Activated T cells were plated onto polyethyleneimine-coated glass coverslips and incubated for 30 min at 37°C with 5 nM potentiometric probe tetramethylrhodamine methyl ester (TMRM; Invitrogen), a lipophilic cationic dye that accumulates in the mitochondrial matrix in the amount proportional to the magnitude of mitochondrial inner membrane potential ($\Delta\Psi_m$) [44], as previously described [45–47]. Coverslips with adherent cells were mounted into a recording chamber and placed on the stage of a Nikon A1 laser scanning confocal microscope (Nikon Instruments Inc.). The recording chamber was continuously perfused with solutions containing 5 nM TMRM. During time-lapse recording, TMRM was excited with a 543-nm laser line, and emission was detected using a 565–605 nm band-path filter. At

the end of each experiment, 10 μM carbonyl cyanide phenyl hydrazone (FCCP) was added to the bath solution to dissipate $\Delta\Psi_m$. Experiments were performed at room temperature in air. Image analysis was performed using Nikon NIS-Elements C software. In each experiment, the TMRM fluorescence intensity values were normalized such that the TMRM fluorescence intensity level recorded 30 min after FCCP application was set to 0, whereas the TMRM fluorescence intensity level before the first solution exchange was set to 1.

2.5. Immunofluorescence.

Staining for RyR was performed as we previously described [11]. Briefly, activated T cells were plated on polyethyleneimine-coated coverslips and fixed with 4% paraformaldehyde in PBS for 30 min, washed three times with 2× PBS, and permeabilized for 1 h in 0.075 (% w/v) saponin solution in 2× PBS. Cells were blocked in 5% (v/v) goat serum and 5% (w/v) bovine serum albumin in 2× PBS for 1 h at 21 °C. Coverslips were incubated overnight at +4 °C with primary mouse mAb 34C (1:10 concentrate dilution; Developmental Studies Hybridoma Bank, University of Iowa, Iowa City, IA), which recognize RyR1 and RyR2 [11, 48, 49]. Mouse IgG1 mAb (Invitrogen) was used as a negative control. Coverslips were washed three times with 2× PBS and goat anti-mouse Alexa Fluor 488-conjugated secondary Ab (1:1000 dilution; Molecular Probes) was applied for 1 h at 21 °C. Cell nuclei were contrast-stained by incubation with 1 μM TO-PRO 3-iodide solution (Molecular Probes) for 5 min before mounting. After washing three times with 2× PBS, the coverslips were mounted on microscope slides in the AntiFade mounting solution (Molecular Probes, Inc.). Fluorescence images of fixed cells were acquired using an LSM 510 laser-scanning confocal microscope (Carl Zeiss). The excitation/emission settings were as follows: 488-nm excitation and 505–550-nm emission filters were used for Alexa Fluor 488; 633-nm excitation and 650-nm long-pass emission filters were used for TO-PRO 3-iodide.

2.6. Classical statistical analyses.

Statistical analyses were performed using Origin 7 software (Origin Lab). Shapiro-Wilk Normality Test was performed before the parametric analyses. For data sets that displayed normality at 0.05 level, the differences between variable means were evaluated using a two-sample Student's *t*-test; the cut-off significance level was set at p-values ≤ 0.05. For multiple comparisons, the p values were ranked using the Benjamini-Hochberg procedure [50] to keep a false discovery rate at ≤ 5% or ≤ 10%, as indicated in figure legends. Unless otherwise indicated, summarized data are presented as a mean ± standard error (SE).

2.7. Machine learning analyses.

Clustering and classification analyses were performed using Orange3 (Version 3.24, https://orange.biolab.si/, Copyright © University of Ljubljana). The genetic background of the samples (HET T cells and WT T cells) was used as the target variable in the example Classification Tree and Cross-Validation workflows included with the software. Data with missing values were excluded from these analyses. For the classification tree building, the following settings were used (Logistic regression Ridge2 rasterization c=1). In the Cross-Validation workflow three learning algorithms were tried: Logistic Regression, Random Forest Classification, and Support Vector Machine [51], all yielding similar results. For the calculation of the confusion matrix reported here, the sampling method settings were

Logistic Regression, random sampling, training set size 66%, repeat train/test 10 times. Calculations for sensitivity and specificity were done using standard equations (1) and (2) as described in [52].

$$\text{sensitivity} = \frac{\text{number of true positives}}{\text{number of true positives} + \text{number of false negatives}} \quad (1)$$

$$\text{specificity} = \frac{\text{number of true negatives}}{\text{number of true negatives} + \text{number of false positives}} \quad (2)$$

3. RESULTS

3.1 Resting WT and HET T cells display similar levels of resting $[Ca^{2+}]_i$ and no difference in their response to store depletion with thapsigargin (Tg) and activation of SOCE.

There was no significant difference in the resting $[Ca^{2+}]_i$ values between resting WT and HET T cells (Fig. 1). Substitution of normal bath solution with nominally Ca^{2+}-free bath solution resulted in a small decline in $[Ca^{2+}]_i$ in both types of cells. Application of Tg, a SERCA blocker, elicited either transient or oscillatory elevation in $[Ca^{2+}]_i$ in the absence of Ca^{2+} in the extracellular solution due to passive Ca^{2+} mobilization from the intracellular store in both WT and HET resting T cells. Re-addition of Ca^{2+}-containing bath solution produced a rapid elevation in $[Ca^{2+}]_i$ due to activation of SOCE, which reached comparable maximal peak $[Ca^{2+}]_i$ levels at a similar rate in both WT and HET T cells (Fig. 1). Thus, there were no significant differences in resting $[Ca^{2+}]_i$ levels or responses to Tg or SOSE between WT and HET T cell, which is consistent with our previous findings that RyR contribution to global $[Ca^{2+}]_i$ dynamics in resting T cells is small compared with that in activated T cells [11].

3.2 Activated HET T cells display elevated resting $[Ca^{2+}]_i$, diminished response to Tg, and reduced rate of $[Ca^{2+}]i$ elevation after activation of SOCE compared with WT T cells.

T cell receptor stimulation triggered the expansion of both WT and HET T cells with a similar doubling time of ~ 48 hours during the logarithmic phase of growth. However, the HET T cells displayed an earlier onset of the stationary phase of growth compared with WT T cells (Fig. 2 A). Both activated WT and HET T cells were positively stained for RyR (Fig. 2 B) but exhibited significant differences in $[Ca^{2+}]_i$ dynamics. Activated HET T cells displayed significantly higher resting $[Ca^{2+}]_i$ levels compared with activated WT T cells (Fig. 3 A & B). Removal of Ca^{2+} from the bath solution resulted in a drop in $[Ca^{2+}]_i$ to about the same level in both HET and WT T cells. Application of Tg in Ca^{2+}-free bath solution elicited $[Ca^{2+}]_i$ transients, which were significantly larger in amplitude in WT T cells compared with those in HET T cells (Fig. 3 A, C & D). Re-addition of Ca^{2+} into bath solution elicited a massive increase in $[Ca^{2+}]_i$ caused by activation of SOCE in both HET and WT activated T cells (Fig. 3 A & E). The maximal rate of $[Ca^{2+}]_i$ elevation following Ca^{2+} re-addition was significantly slower in HET T cells compared with WT T cells (Fig. 3 E & F), whereas peak values of $[Ca^{2+}]_i$ elevation following SOCE activation were not significantly different between HET and WT T cells (Fig. 2 G).

Pre-incubation with Ry (400 μM) or DS (50 μM) for 30 min significantly reduced the basal $[Ca^{2+}]_i$ and increased the magnitude of Tg-elicited $[Ca^{2+}]_i$ transients in HET T cells (Fig. 3 A – D). Preincubation with Ry also increased the rate of $[Ca^{2+}]_i$ elevation following Ca^{2+} re-addition in HET T cells (Fig. 3 E & F). Thus, mitigating effects of RyR blockers indicate the involvement of RyR1 in disparities in resting $[Ca^{2+}]_i$ levels, Tg-evoked Ca^{2+} transients, and rate of SOCE between WT and HET T cells. The magnitude of $[Ca^{2+}]_i$ elevation following SOCE activation was not significantly different among WT T cells, HET T cells, and HET T cells preincubated with Ry (Fig. 3 G). The peak $[Ca^{2+}]_i$ following SOCE activation was reduced in HET T cells preincubated with DS compared with WT T cells, which may be caused by direct suppression of SOCE by DS [53].

3.3. Activated R163C HET and WT T cells display different changes in $\Delta\Psi_m$ in response to SOCE.

We further explored whether perturbation of $[Ca^{2+}]_i$ differentially affects mitochondrial function in activated WT and HET T cells by monitoring changes in $\Delta\Psi_m$ in response to variations in $[Ca^{2+}]_i$. After loading with TMRM, both WT and HET activated T cells displayed punctate fluorescence signal consistent with the mitochondrial localization of the dye (Fig. 4 A). Removal of Ca^{2+} from bath solution, which prompts a decline in $[Ca^{2+}]_i$ (Fig. 3 A), elicited a decline in TMRM fluorescence intensity in the puncta in both WT and HET T cells (Figure 4 A, B), indicating $\Delta\Psi_m$ depolarization, which was followed by a slow increase in TMRM fluorescence after application of Tg, indicating $\Delta\Psi_m$ hyperpolarization. Re-addition of extracellular Ca^{2+}, which elicited SOCE (Fig. 3 A), produced either sustained or transient decline in TMRM fluorescence, indicating $\Delta\Psi_m$ depolarization in WT T cells (Fig. 4 A–C). In contrast, the re-addition of extracellular Ca^{2+} to the activated HET T cells produced a progressive elevation in TMRM fluorescence, indicating $\Delta\Psi_m$ hyperpolarization. Differences in the TMRM fluorescence intensities between WT and HET T cells became significant within 1 minute after initiation of SOCE. Integrals of changes in $\Delta\Psi_m$ during the first 4 minutes after re-addition of extracellular Ca^{2+} were significantly different in HET T cells compared with WT T cells (Fig. 4 D). Removal of bath Ca^{2+} after SOCE activation elicited a reduction in TMRM fluorescence in both WT and HET T cells (Fig. 4 A, B), whereas application of FCCP, which dissipates the $\Delta\Psi_m$, resulted in a typical decay profile of TMRM fluorescence.

3.4. Machine learning analyses of $[Ca^{2+}]_i$ and $\Delta\Psi_m$ variables can separate and predict the genotype of activated T cells.

We have used a machine learning approach to identify significant variables measured in the experiments presented in Figures 3 and 4 for association with the HET or WT genotype and to test the hypothesis that these variables can correctly classify activated T cells as having a specific genetic background (HET or WT). Because values of the resting $[Ca^{2+}]_i$ (Fig. 3 B) and magnitude of Tg-evoked $[Ca^{2+}]_i$ transients (Fig. 3 D) deviated in different directions in HET and WT cells, we took the ratio of these two values as an additional variable for the exploratory analyses.

Exploratory data analysis with a machine learning algorithm optimizing genotype-associated differences revealed that data sets obtained from HET and WT T cells can be separated

when using the amplitude of the Tg-evoked $[Ca^{2+}]_i$ transients (Fig. 3 D), the ratio of resting $[Ca^{2+}]_i$ to the amplitude of the Tg-evoked $[Ca^{2+}]_i$ transients (Fig. 3 B and D), or integral of changes in $\Delta\Psi_m$ during the first 4 minutes after re-addition of extracellular Ca^{2+} (Fig. 4 C) as single-label classification variables (Fig. 5 A). Using the resting $[Ca^{2+}]_i$ (Fig. 3 B), or rate of the $[Ca^{2+}]_i$ elevation following SOCE activation (Fig. 3 G), as single-label classification variables did not produce a clear separation between HET and WT genotype classes (Supplementary Figure 2). However, by using them as a pair it was possible to resolve the genotype classes.

The classification trees show that the HET and WT genotype classes can be classified correctly with 100% accuracy using the amplitude of the Tg-evoked $[Ca^{2+}]_i$ transient, integral of $\Delta\Psi_m$, or ratio of resting $[Ca^{2+}]_i$ to the amplitude of the Tg-evoked $[Ca^{2+}]_i$ transients (Fig. 5 B). Cells cannot be classified into HET and WT genotype classes with 100% accuracy using resting $[Ca^{2+}]_i$ or rate of $[Ca^{2+}]_i$ elevation after SOCE activation as single-label classification variables (Supplemental Figure 2). However, 100% accuracy can be achieved when using the combination of these two variables. Application of Logistic Regression, Random Forest Classification, and Support Vector Machine Learning algorithms produced similar outcomes (not shown). We then examined the likelihood that a random set of data would be classified correctly by our system of variables using logistic regression. The best predictive outcome was obtained when the amplitude of the Tg-evoked $[Ca^{2+}]_i$ transient was used as a single-label classification variable (the error rate (0%), accuracy (100%), sensitivity (100%) and specificity (100%)). When all three significant single-label classification variables were used, the error rate (3%), accuracy (97%), sensitivity (100%), and specificity (93%) were calculated from the confusion matrix (Fig. 5C).

5. DISCUSSION

Here we report that *RyR1*-p.R163C mutation, which has been associated with debilitating skeletal muscle diseases in humans, causes aberrations in intracellular Ca^{2+} signaling and mitochondrial function in activated murine T lymphocytes. Activated HET T cells displayed elevated resting $[Ca^{2+}]_i$ compared with WT T cells. This finding is consistent with previously reported elevation in basal $[Ca^{2+}]_i$ in skeletal muscle and B lymphocytes from MH-susceptible humans and pre-clinical animal models of MH, including HET R163C mice, compared with MH non-susceptible individuals and WT animals [22, 25–31, 54, 55]. A previous study on muscle cells from HET R163C knock-in mice has shown that elevation in resting $[Ca^{2+}]_i$ in those cells is due to an augmented influx of sarcolemmal Ca^{2+} at rest [26]. It was also shown that responses to RyR agonists caffeine and 4-chloro-m-cresol were augmented in B cells derived from MH-susceptible individuals compared with B cells derived from MH-negative controls [56, 57], although specific pathways responsible for such augmentation remain unexplored.

In the present study, application of Tg in Ca^{2+}-free solution elicited significantly smaller amplitude $[Ca^{2+}]_i$ transients in activated HET T cells compared with WT T cells. This effect may be attributed to either the partial store depletion due to the increased Ca^{2+} leakage from the RyR1 and/or upregulation of Ca^{2+} extrusion mechanisms in the presence of elevated resting $[Ca^{2+}]_i$ in activated HET T cells. Application of Ry or DS reduced basal $[Ca^{2+}]_i$ and

augmented the response to Tg in activated HET T cells, indicating that both the elevation in resting $[Ca^{2+}]_i$ and diminished response to Tg in activated HET T cells are due to the enhanced Ca^{2+} leakage from the RyR1. There were no significant differences in $[Ca^{2+}]_i$ dynamics between resting HET and WT T cells, consistent with previous findings that RyR1 do not contribute significantly to global Ca^{2+} signaling in these cells [11], although RyR1 are involved in the formation ofCa^{2+} microdomains in resting T cells following T cell receptor stimulation [12].

We found that activated HET T cells displayed slower kinetics of $[Ca^{2+}]_i$ elevation after activation of SOCE compared with WT activated T cells. This effect cannot be directly caused by Ca^{2+} leakage from the RyR1 in HET T cells because Tg irreversibly depletes the store before activation of SOCE, thereby diminishing Ca^{2+}-induced Ca^{2+} release from the RyR1 during SOCE in both HET and WT cells. One possible explanation for the delayed kinetics of Ca^{2+} elevation in activated HET cells compared with WT T cells is that chronic elevation in resting $[Ca^{2+}]_i$ results in compensatory upregulation of Ca^{2+} extrusion mechanisms, which hamper $[Ca^{2+}]_i$ elevation after SOCE activation in HET T cells. Another possibility is that the gain-of-function of RyR1 affects the gating properties of the plasmalemmal store-operated channels mediating SOCE. Under physiological conditions, delayed kinetics of SOCE may affect the dynamics of T cell Ca^{2+} signaling, such as the patterns of Ca^{2+} oscillations.

Effects of RyR blockers indicate that observed differences between WT and HET T cells in resting $[Ca^{2+}]_i$, $[Ca^{2+}]_i$ responses to Tg, and rate of $[Ca^{2+}]_i$ elevation following activation of SOCE are directly or indirectly caused by the increased Ca^{2+} discharge from the RyR1 in HET cells. The magnitude of $[Ca^{2+}]_i$ elevation following SOCE activation was not significantly different among WT T cells, HET T cells, and HET T cells preincubated with Ry, which is likely caused by the failure of high-affinity Ca^{2+} indicator Fura 2 to correctly report $[Ca^{2+}]_i$ in micromolar range of $[Ca^{2+}]$. A decline in the rate and magnitude of $[Ca^{2+}]_i$ elevation after SOCE activation in HET T cells preincubated with DS compared with WT T cells can be attributed to the direct effect of DS on SOCE described previously [53].

To assess mitochondrial function, we employed a cationic probe TMRM, which primarily reports changes in $\Delta\Psi_m$ but also may be influenced by the plasma membrane potential [58]. Previous studies performed on the cardiomyocytes [45], 143B osteosarcoma cells [59] shown that under the loading conditions used in our study, most of the TMRM accumulates in the mitochondria. In the present study, we observed that TMRM-loaded HET and WT T cells displayed a punctate fluorescence signal similar to that produced by a lipophilic mitochondrial-selective dye DiOC6 previously described in the primary human T cells [60]. Thus, an apparent mitochondrial localization of the TMRM indicates that changes in TMRM fluorescence intensity are primarily due to changes in the $\Delta\Psi_m$ in both HET and WT T cells.

Small deviations in $[Ca^{2+}]_i$ levels induced by removal of extracellular Ca^{2+} or subsequent intracellular Ca^{2+} mobilization with Tg produced similar effects on $\Delta\Psi_m$ in both WT and HET activated T cells. Removal of cytosolic Ca^{2+} dissipated $\Delta\Psi_m$ in both WT and HET cells, presumably due to the reduction of mitochondrial Ca^{2+} uptake occurring at nanomolar cytosolic Ca^{2+} levels and accompanying suppression of respiratory chain reactions, which

maintains $\Delta\Psi_m$ [61, 62]. The $\Delta\Psi_m$ was partially restored after Tg-induced Ca^{2+} mobilization from the store in both WT and HET T cells. Interestingly, while Tg application in nominally Ca^{2+}-free bath solution elicited much smaller elevation in global $[Ca^{2+}]_i$ in activated HET T cells compared with WT T cells, it evoked similar increases in $\Delta\Psi_m$ in both HET and WT T cells. Given that in activated T cells mitochondria and endoplasmic reticulum are located in close apposition [63], and that functional coupling between these organelles has been established [64, 65], local signaling between endoplasmic reticulum and mitochondria is likely responsible for Tg-induced changes in $\Delta\Psi_m$ in both HET and WT T cells that are largely unaffected by small variations in global $[Ca^{2+}]_i$.

The $\Delta\Psi_m$ was differentially affected by SOCE in HET and WT activated T cells. In WT cells, SOCE predominantly elicited dissipation of $\Delta\Psi_m$ during the first several minutes after SOCE activation, whereas in HET cells, activation of SOCE hyperpolarized the $\Delta\Psi_m$. It has been shown that depending on the magnitude, mitochondrial Ca^{2+} uptake may elicit either $\Delta\Psi_m$ hyperpolarization, which promotes Ca^{2+} clearance from the cytosol, or transient or sustained dissipation of $\Delta\Psi_m$, which may prevent mitochondrial Ca^{2+} overload and activation of death pathways [19, 62, 64, 66–68]. Thus, transient or sustained dissipation of $\Delta\Psi_m$ in WT T cells observed in our study is likely due to mitochondrial Ca^{2+} overload caused by the large magnitude of SOCE. It is not clear why SOCE of a comparable magnitude elicited $\Delta\Psi_m$ hyperpolarization in HET cells but $\Delta\Psi_m$ depolarization in WT cells. One possible explanation is the mitochondrial metabolic adaptation to chronic elevation of extramitochondrial Ca^{2+}, which may result in enhanced Ca^{2+} sequestration capacity of HET T cell mitochondria compared with WT T cell mitochondria, which in turn causes $\Delta\Psi_m$ hyperpolarization and enhancement of mitochondrial energetics in response to SOCE in HET T cells [64, 67, 68].

Increased Ca^{2+} accumulation in the skeletal muscle mitochondrial matrix of HET R163C and Y522S-RYR1 mice compared with WT mice, has been previously reported [32, 35]. Changes in mitochondrial function and cellular metabolic activity were also shown in B lymphocytes from MH susceptible individuals [55]. Taken together, these data indicate that MH-associated mutations in *RYR1* may elicit defects in mitochondrial function not only in the skeletal muscle but also in T and B lymphocytes. Although mitochondrial dysfunction in the skeletal muscle may account for some symptoms of MH (e.g. metabolic acidosis and hyperthermia), further studies are necessary to delineate the effects of mitochondrial dysfunction in lymphocytes.

In T cells, elevation in $[Ca^{2+}]_i$, drives major T cell effector functions, such as gene expression program, proliferation, and cytokine production, via activation of Ca^{2+}-calmodulin-dependent phosphatase calcineurin and nuclear factor of activated T cells (NFAT) transcription factors [69, 70]. Effects of RyR1 modulation on local and global Ca^{2+} signaling were shown in WT human [11] and mouse [12] primary T cells *in vitro*. It was reported that RyR blockade attenuated SOCE and reduced the rate of proliferation and cytokine production in human T cells *in vitro* [9, 11]. Another study reported downregulation of the calcineurin/NFAT pathway in the skeletal muscle of R163C mice expressing “leaky” RyR1, which ironically coincided with chronic elevation in resting $[Ca^{2+}]_i$, [32]. In this study, we observed that HET T cells display an earlier onset of the

stationary phase of growth compared with WT T cells, which may be due to a decline in mitotic index [71] caused by downregulation of the calcineurin/NFAT pathway, and/or acceleration of the activation-induced T cell death [72] facilitated by mitochondrial hyperpolarization [73]. Thus, modulation of RyR1 function, both gain-of-function and down-regulation, regulate T cell effector functions and may affect the immune response *in vivo*. Indeed, knock-in mice heterozygously expressing gain-of-function *RYR1* mutation Y522S, display subtle but significant differences in basal levels of immune markers and strength of triggered specific immune responses compared with WT mice [74]. Because deletion of RyR1 in mice leads to perinatal lethality [75], the knock-in mice expressing the gain-of-function RyR1 mutations represent a convenient model for future elucidation of the role of RyR1 in immune responses *in vivo*.

Statistical learning analyses of the predictive model generated from the empirically measurable variables obtained from HET and WT activated T cells indicate that these variables can be used as the physiological markers to correctly classify activated T cells as having a specific genotype (HET or WT). When used as the classification variable, the amplitude of Ca^{2+} transient evoked by Tg showed the best promise in predicting the presence of *RyR1*-p.R163C mutation, displaying 100% sensitivity and 100% specificity. The combination of other parameters also yielded high specificity and sensitivity results, indicating that they also can be used for sample identification. Our estimates of sensitivity and specificity should be considered with caution given the limited sample size used in this study and should be verified on a larger data set to increase the rigor. Because *RyR1*-p.R163C mutation causes gain-of-function of RyR1, the approach described here can be used to classify activated T cells having inherited RyR1 hyperfunction. Thus, we have established proof of principle for the *in vitro* T cell-based diagnostic assay for RyR1 hyperfunction, which uses a set of well-established, easily measurable cellular response variables that have an innate ability to report RyR1 functional impairment. Given complex variations in genetic and environmental factors underlying the diseases associated with RyR1 dysfunction [76, 77], a more complex model integrating heterogeneous data from different types of tests [78] needs to be developed to diagnose a disease and predict treatment outcomes in a real-world context.

Supplementary Material

Refer to Web version on PubMed Central for supplementary material.

Acknowledgments

We would like to thank Associate Professor Athena Soulika, Ph.D., Department of Dermatology, University of California Davis, Davis, CA, USA, for help with murine T cell isolation: Professor Isaac Pessah, Ph. D, Professor Jon Ramsey, Ph.D., and Assistant Project Scientist Jennifer Rutkowsky, Ph.D., Department of Molecular Biosciences, University of California Davis, Davis, CA, USA, for providing genotyped mice.

Funding Sources

UC Davis School of Medicine Research Partnership Grant (to AFF); University of California Innovative Development Award (to END); NIH 1R01AR068897 (to PDA).

Abbreviations:

RyR	ryanodine receptors
RyR1	ryanodine receptors type 1
MH	malignant hyperthermia
HET R163C mice	mice heterozygous for human *RYR1* N-terminal mutation p.R163C
HET T cells	T cells isolated from lymphoid organs of HET R163C mice
WT mice	wild-type mice
WT T cells	T cells isolated from lymphoid organs of WT mice
$[Ca^{2+}]_i$	cytosolic Ca^{2+} concentration
PHA	phytohemagglutinin P
TMRM	tetramethylrhodamine methyl ester
FCCP	carbonyl cyanide phenyl hydrazone
SOCE	store-operated Ca^{2+} entry
Tg	thapsigargin
Ry	ryanodine
DS	dantrolene sodium
$\Delta\Psi m$	mitochondrial membrane potential

References

1. Lawal TA, et al., Ryanodine receptor 1-related disorders: an historical perspective and proposal for a unified nomenclature. Skelet Muscle, 2020 10 (1): p. 32. [PubMed: 33190635]
2. Yang L, et al., The current status of malignant hyperthermia. J Biomed Res, 2019 34(2): p. 75–85. [PubMed: 32305961]
3. Fokkema IF, et al., LOVD v.2.0: the next generation in gene variant databases. Hum Mutat, 2011 32(5): p. 557–63. [PubMed: 21520333]
4. Riazi S, Kraeva N, and Hopkins PM, Malignant Hyperthermia in the Post-Genomics Era: New Perspectives on an Old Concept. Anesthesiology, 2018 128 (1): p. 168–180. [PubMed: 28902675]
5. Rosenberg H, et al., Malignant hyperthermia: a review. Orphanet J Rare Dis, 2015 10:p. 93. [PubMed: 26238698]
6. Hopkins PM, et al., European Malignant Hyperthermia Group guidelines for investigation of malignant hyperthermia susceptibility. Br J Anaesth, 2015 115 (4): p. 531–9. [PubMed: 26188342]
7. Dammermann W, et al., NAADP-mediated Ca2+ signaling via type 1 ryanodine receptor in T cells revealed by a synthetic NAADP antagonist. Proc Natl Acad Sci U S A, 2009 106 (26): p. 10678–83. [PubMed: 19541638]
8. Gao J, et al., Ryanodine receptor-mediated rapid increase in intracellular calcium induced by 7,8-benzo(a)pyrene quinone in human and murine leukocytes. Toxicol Sci, 2005 87 (2): p. 419–26. [PubMed: 16049270]

9. Conrad DM, et al., Ryanodine receptor signaling is required for anti-CD3-induced T cell proliferation, interleukin-2 synthesis, and interleukin-2 receptor signaling. J Cell Biochem, 2004 92 (2): p. 387–99. [PubMed: 15108363]
10. Hosoi E, et al., Expression of the ryanodine receptor isoforms in immune cells. J Immunol, 2001 167(9): p. 4887–94. [PubMed: 11673493]
11. Thakur P, Dadsetan S, and Fomina AF, Bidirectional coupling between ryanodine receptors and Ca2+ release-activated Ca2+ (CRAC) channel machinery sustains store-operated Ca2+ entry in human T lymphocytes. J Biol Chem, 2012 287 (44): p. 37233–44. [PubMed: 22948152]
12. Diercks BP, et al., ORAI1, STIM1/2, and RYR1 shape subsecond Ca(2+) microdomains upon T cell activation. Sci Signal, 2018 11(561).
13. Dadsetan S, et al., Store-operated Ca2+ influx causes Ca2+ release from the intracellular Ca2+ channels that is required for T cell activation. J Biol Chem, 2008 283 (18): p. 12512–9. [PubMed: 18316371]
14. Huttemann M, et al., Regulation of oxidative phosphorylation, the mitochondrial membrane potential, and their role in human disease. J Bioenerg Biomembr, 2008 40(5): p. 445–56. [PubMed: 18843528]
15. Zorova LD, et al., Mitochondrial membrane potential. Anal Biochem, 2018 552: p. 50–59. [PubMed: 28711444]
16. Csordas G, Weaver D, and Hajnoczky G, Endoplasmic Reticulum-Mitochondrial Contactology: Structure and Signaling Functions. Trends Cell Biol, 2018 28(7): p. 523–540. [PubMed: 29588129]
17. Rizzuto R, et al., Mitochondria as sensors and regulators of calcium signalling. Nat Rev Mol Cell Biol, 2012 13(9): p. 566–78. [PubMed: 22850819]
18. Hajnoczky G, Csordas G, and Yi M, Old players in a new role: mitochondria-associated membranes, VDAC, and ryanodine receptors as contributors to calcium signal propagation from endoplasmic reticulum to the mitochondria. Cell Calcium, 2002 32(5–6): p. 363–77. [PubMed: 12543096]
19. Williams GS, et al., Mitochondrial calcium uptake. Proc Natl Acad Sci U S A, 2013 110(26): p. 10479–86. [PubMed: 23759742]
20. Quane KA, et al., Mutations in the ryanodine receptor gene in central core disease and malignant hyperthermia. Nat Genet, 1993 5(1): p. 51–5. [PubMed: 8220423]
21. Mungunsukh O, et al., Estimating prevalence of malignant hyperthermia susceptibility through population genomics data. Br J Anaesth, 2019 123(3): p. e461–e463. [PubMed: 31301762]
22. Yang T, et al., Pharmacologic and functional characterization of malignant hyperthermia in the R163C RyR1 knock-in mouse. Anesthesiology, 2006 105(6): p. 1164–75. [PubMed: 17122579]
23. Lawal TA, et al., Preclinical model systems of ryanodine receptor 1-related myopathies and malignant hyperthermia: a comprehensive scoping review of works published 1990–2019. Orphanet J Rare Dis, 2020 15(1): p. 113. [PubMed: 32381029]
24. Fusto A, et al., Cored in the act: the use of models to understand core myopathies. Dis Model Mech, 2019 12(12).
25. Feng W, et al., Functional and biochemical properties of ryanodine receptor type 1 channels from heterozygous R163C malignant hyperthermia-susceptible mice. Mol Pharmacol, 2011 79(3): p. 420–31. [PubMed: 21156754]
26. Eltit JM, et al., Nonspecific sarcolemmal cation channels are critical for the pathogenesis of malignant hyperthermia. FASEB J, 2013 27(3): p. 991–1000. [PubMed: 23159934]
27. Yuen B, et al., Mice expressing T4826I-RYR1 are viable but exhibit sex- and genotype-dependent susceptibility to malignant hyperthermia and muscle damage. Faseb J, 2012 26(3): p. 1311–22. [PubMed: 22131268]
28. Zullo A, et al., Voltage modulates halothane-triggered Ca(2+) release in malignant hyperthermia-susceptible muscle. J Gen Physiol, 2018 150(1): p. 111–125. [PubMed: 29247050]
29. Lopez JR, et al., Effects of dantrolene on myoplasmic free [Ca2+] measured in vivo in patients susceptible to malignant hyperthermia. Anesthesiology, 1992 76(5): p. 711–9. [PubMed: 1575338]
30. Figueroa L, et al., Abnormal calcium signalling and the caffeine-halothane contracture test. Br J Anaesth, 2019 122(1): p. 32–41. [PubMed: 30579404]

31. Lopez JR, et al., Enhanced response to caffeine and 4-chloro-m-cresol in malignant hyperthermia-susceptible muscle is related in part to chronically elevated resting [Ca2+]i. Am J Physiol Cell Physiol, 2005 288(3): p. C606–12. [PubMed: 15537710]
32. Giulivi C, et al., Basal bioenergetic abnormalities in skeletal muscle from ryanodine receptor malignant hyperthermia-susceptible R163C knock-in mice. J Biol Chem, 2011 286(1): p. 99–113. [PubMed: 20978128]
33. Barrientos GC, et al., Gene dose influences cellular and calcium channel dysregulation in heterozygous and homozygous T4826I-RYR1 malignant hyperthermia-susceptible muscle. J Biol Chem, 2012 287(4): p. 2863–76. [PubMed: 22139840]
34. Chang L, et al., Bioenergetic defects in muscle fibers of RYR1 mutant knock-in mice associated with malignant hyperthermia. J Biol Chem, 2020 295(45): p. 15226–15235. [PubMed: 32826313]
35. Canato M, et al., Excessive Accumulation of Ca(2 +) in Mitochondria of Y522S-RYR1 Knock-in Mice: A Link Between Leak From the Sarcoplasmic Reticulum and Altered Redox State. Front Physiol, 2019 10: p. 1142. [PubMed: 31607937]
36. Friedmann KS, Bozem M, and Hoth M, Calcium signal dynamics in T lymphocytes: Comparing in vivo and in vitro measurements. Semin Cell Dev Biol, 2019 94: p. 84–93. [PubMed: 30630031]
37. Masopust D, Sivula CP, and Jameson SC, Of Mice, Dirty Mice, and Men: Using Mice To Understand Human Immunology. J Immunol, 2017 199(2): p. 383–388. [PubMed: 28696328]
38. Lim JF, Berger H, and Su IH, Isolation and Activation of Murine Lymphocytes. J Vis Exp, 2016(116).
39. Nowell PC, Phytohemagglutinin: an initiator of mitosis in cultures of normal human leukocytes. Cancer Res, 1960 20: p. 462–6. [PubMed: 14427849]
40. Vancha AR, et al., Use of polyethyleneimine polymer in cell culture as attachment factor and lipofection enhancer. BMC Biotechnol, 2004 4: p. 23. [PubMed: 15485583]
41. Bruil A, et al., In vitro leucocyte adhesion to modified polyurethane surfaces. I. Effect of ionizable functional groups. Biomaterials, 1992 13(13): p. 915–23. [PubMed: 1477260]
42. Grynkiewicz G, Poenie M, and Tsien RY, A new generation of Ca2+ indicators with greatly improved fluorescence properties. J Biol Chem, 1985 260(6): p. 3440–50. [PubMed: 3838314]
43. Fanger CM, Neben AL, and Cahalan MD, Differential Ca2+ influx, KCa channel activity, and Ca2+ clearance distinguish Th1 and Th2 lymphocytes. J Immunol, 2000 164(3): p. 1153–60. [PubMed: 10640725]
44. Ehrenberg B, et al., Membrane potential can be determined in individual cells from the nernstian distribution of cationic dyes. Biophys J, 1988 53(5): p. 785–94. [PubMed: 3390520]
45. Dedkova EN and Blatter LA, Measuring mitochondrial function in intact cardiac myocytes. J Mol Cell Cardiol, 2012 52(1): p. 48–61. [PubMed: 21964191]
46. Seidlmayer LK, et al., Distinct mPTP activation mechanisms in ischaemia-reperfusion: contributions of Ca2+, ROS, pH, and inorganic polyphosphate. Cardiovasc Res, 2015 106(2): p. 237–48. [PubMed: 25742913]
47. Seidlmayer LK, et al., Inositol 1,4,5-trisphosphate-mediated sarcoplasmic reticulum-mitochondrial crosstalk influences adenosine triphosphate production via mitochondrial Ca2+ uptake through the mitochondrial ryanodine receptor in cardiac myocytes. Cardiovasc Res, 2016 112(1): p. 491–501. [PubMed: 27496868]
48. Li P and Chen SR, Molecular basis of Ca(2)+ activation of the mouse cardiac Ca(2)+ release channel (ryanodine receptor). J Gen Physiol, 2001 118(1): p. 33–44. [PubMed: 11429443]
49. Du GG, Imredy JP, and MacLennan DH, Characterization of recombinant rabbit cardiac and skeletal muscle Ca2+ release channels (ryanodine receptors) with a novel [3H]ryanodine binding assay. J Biol Chem, 1998 273(50): p. 33259–66. [PubMed: 9837897]
50. Benjamini Y and Hochberg Y, Controlling the false discovery rate: a practical and powerful approach to multiple testing. Journal of the Royal Statistical Society, Series B (Statistical Methodology), 1995 57(1): p. 289–300.
51. James G, et al., An Introduction to Statistical Learningwith Applications in R 8th ed. Springer Texts in Statistics (Book 103), ed. Casella G, Fienberg S, and Olkin I. 2017: Springer 440.
52. Miecznikowski JC and Sellers KF, Statistical Analysis of Chemical Sensor Data Advances in Chemical Sensors., ed. Wang W. 2012: IntechOpen.

53. Zhao X, et al., Azumolene inhibits a component of store-operated calcium entry coupled to the skeletal muscle ryanodine receptor. J Biol Chem, 2006 281(44): p. 33477–86. [PubMed: 16945924]
54. Zhou J, et al., Malignant Hyperthermia and Other Related Disorders, in Miller's Anesthesia, 9th ed. 1918, Elsevier Health Sciences New York.
55. Johannsen S, et al., Functional characterization of the RYR1 mutation p.Arg4737Trp associated with susceptibility to malignant hyperthermia. Neuromuscul Disord, 2016 26(1): p. 21–5. [PubMed: 26631338]
56. Perry SM, et al., Effect of Norepinephrine on Intracellular Ca(2+) Levels in Malignant Hyperthermia-Susceptible B Cells: Pilot Study in the Search for a New Diagnostic Test for Malignant Hyperthermia. AANA J, 2018 86(5): p. 383–392. [PubMed: 31584408]
57. Sei Y, et al., Patients with malignant hyperthermia demonstrate an altered calcium control mechanism in B lymphocytes. Anesthesiology, 2002 97(5): p. 1052–8. [PubMed: 12411786]
58. Nicholls DG, Simultaneous monitoring of ionophore- and inhibitor-mediated plasma and mitochondrial membrane potential changes in cultured neurons. J Biol Chem, 2006 281(21): p. 14864–74. [PubMed: 16551630]
59. McKenzie M, Lim SC, and Duchen MR, Simultaneous Measurement of Mitochondrial Calcium and Mitochondrial Membrane Potential in Live Cells by Fluorescent Microscopy. J Vis Exp, 2017(119).
60. Fomina AF, et al., Regulation of membrane trafficking and subcellular organization of endocytic compartments revealed with FM1–43 in resting and activated human T cells. Exp Cell Res, 2003 291(1): p. 150–66. [PubMed: 14597416]
61. Santo-Domingo J and Demaurex N, Calcium uptake mechanisms of mitochondria. Biochim Biophys Acta, 2010 1797(6–7): p. 907–12. [PubMed: 20079335]
62. Valero RA, et al., The role of mitochondrial potential in control of calcium signals involved in cell proliferation. Cell Calcium, 2008 44(3): p. 259–69. [PubMed: 18241916]
63. Dadsetan S, Shishkin V, and Fomina AF, Intracellular Ca(2+) release triggers translocation of membrane marker FM1–43 from the extracellular leaflet of plasma membrane into endoplasmic reticulum in T lymphocytes. J Biol Chem, 2005 280(16): p. 16377–82. [PubMed: 15710604]
64. Belosludtsev KN, et al., Mitochondrial Ca2+ Transport: Mechanisms, Molecular Structures, and Role in Cells. Biochemistry (Mosc), 2019 84(6): p. 593–607. [PubMed: 31238859]
65. Tepikin AV, Mitochondrial junctions with cellular organelles: Ca(2+) signaling perspective. Pflugers Arch, 2018 470(8): p. 1181–1192. [PubMed: 29982949]
66. Bernardi P, Mitochondria in muscle cell death. Ital J Neurol Sci, 1999 20(6): p. 395–400. [PubMed: 10937859]
67. Gunter TE, et al., Calcium and mitochondria. FEBS Lett, 2004 567(1): p. 96–102. [PubMed: 15165900]
68. Murgia M, et al., Controlling metabolism and cell death: at the heart of mitochondrial calcium signalling. J Mol Cell Cardiol, 2009 46(6): p. 781–8. [PubMed: 19285982]
69. Trebak M and Kinet JP, Calcium signalling in T cells. Nat Rev Immunol, 2019 19(3): p. 154–169. [PubMed: 30622345]
70. Lewis RS, Calcium oscillations in T-cells: mechanisms and consequences for gene expression. Biochem Soc Trans, 2003 31(Pt 5): p. 925–9. [PubMed: 14505450]
71. Watanabe I and Okada S, Stationary phase of cultured mammalian cells (L5178Y). J Cell Biol, 1967 35(2): p. 285–94. [PubMed: 6055989]
72. Genestier L, Bonnefoy-Berard N, and Revillard JP, Apoptosis of activated peripheral T cells. Transplant Proc, 1999 31(1–2A): p. 33S–38S. [PubMed: 10078225]
73. Nagy G, et al., Nitric oxide, mitochondrial hyperpolarization, and T cell activation. Free Radic Biol Med, 2007 42(11): p. 1625–31. [PubMed: 17462531]
74. Vukcevic M, et al., Gain of function in the immune system caused by a ryanodine receptor 1 mutation. J Cell Sci, 2013 126(Pt 15): p. 3485–92. [PubMed: 23704352]

75. Takeshima H, et al., Excitation-contraction uncoupling and muscular degeneration in mice lacking functional skeletal muscle ryanodine-receptor gene. Nature, 1994 369(6481): p. 556–9. [PubMed: 7515481]

76. Kushnir A, et al., Intracellular calcium leak as a therapeutic target for RYR1-related myopathies. Acta Neuropathol, 2020 139(6): p. 1089–1104. [PubMed: 32236737]

77. Kushnir A, Wajsberg B, and Marks AR, Ryanodine receptor dysfunction in human disorders. Biochim Biophys Acta Mol Cell Res, 2018 1865(11 Pt B): p. 1687–1697. [PubMed: 30040966]

78. Zitnik M, et al., Machine Learning for Integrating Data in Biology and Medicine: Principles, Practice, and Opportunities. Inf Fusion, 2019 50: p. 71–91. [PubMed: 30467459]

79. Marx A, et al., EDISON-WMW: Exact Dynamic Programing Solution of the Wilcoxon-Mann-Whitney Test. Genomics Proteomics Bioinformatics, 2016 14(1): p. 55–61. [PubMed: 26829645]

Highlights

- *RyR1*-p.R163C mutation in ryanodine receptor 1 causes skeletal muscle diseases
- T cells from *RyR1*-p.R163C knock-in mice display atypical cytosolic calcium signaling
- T cells with *RyR1*-p.R163C mutation have an atypical mitochondrial potential response
- Machine learning found classification variables predicting disease-causing genotype
- *RyR1*-p.R163C mutation in T cells may cause aberrations in the immune response

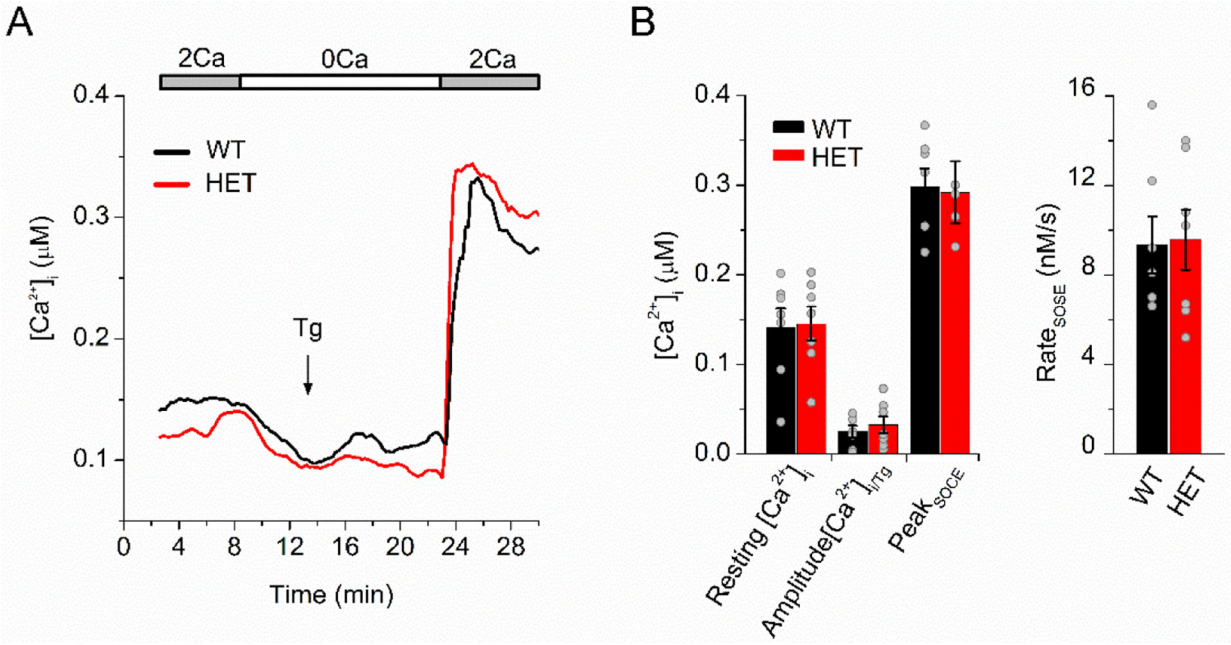

Figure 1. Resting WT and HET T cells display similar changes in $[Ca^{2+}]_i$ in response to changes in extracellular Ca^{2+} concentration and application of Tg.

A, Changes in $[Ca^{2+}]_i$ recorded from activated WT (black trace) and HET (red trace) T cells recorded in representative experiments. Each trace is an average of 12–20 traces from single cells recorded in one experiment. 2 mM Ca^{2+}-containing (2Ca) and nominally Ca^{2+}-free (0Ca) solutions were applied as indicated by horizontal bars; the timing of application of Tg (1 μM) is indicated with an arrow.

B, Values of resting $[Ca^{2+}]_i$ measured as an average level of $[Ca^{2+}]_i$ within 4 min after beginning of the experiment (left panel; Resting $[Ca^{2+}]_i$), magnitudes of Tg-elicited $[Ca^{2+}]_i$ transients (left panel; Amplitude $[Ca^{2+}]_{i/Tg}$, measured as sown in Fig. 3C), and maximal levels of $[Ca^{2+}]_i$ following Ca^{2+} re-addition (left panel; $Peak_{SOCE}$) and maximum rates of $[Ca^{2+}]_i$ elevation following Ca^{2+} re-addition (light panel; $Rate_{SOCE}$, determined as shown in Fig. 3E) recorded from WT (black bars) and HET (red bars) resting T cells. Each circle overlaid on the bar graphs is an average pooled result recorded from 12–20 cells in an individual experiment. Data are from 7 WT and 7 HET mice.

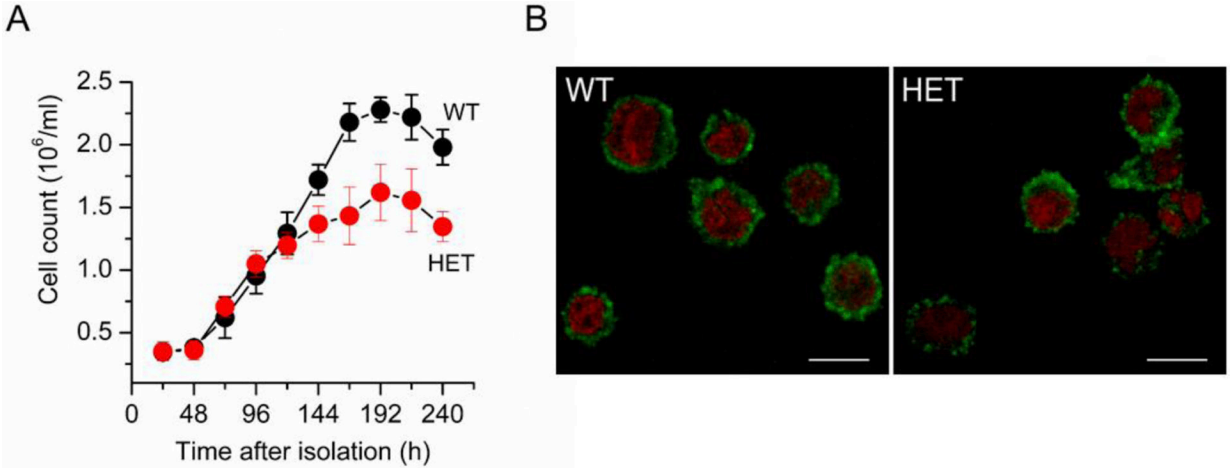

Figure 2. Activated T cell expansion and RyR1 expression.

A, Numbers of activated WT (black circles; n= 4; data from 3 mice) and HET (black circles; n= 6; data from 3 mice) T cells. Cells were activated with PHA on day 0.

B, Anti-RyR immunoreactivity (*green*) in WT (*left panel*) and HET (*right panel*) T cells. Cells were stained 96 hours after activation. Cell nuclei are stained with red. Scale bars, 10 μm.

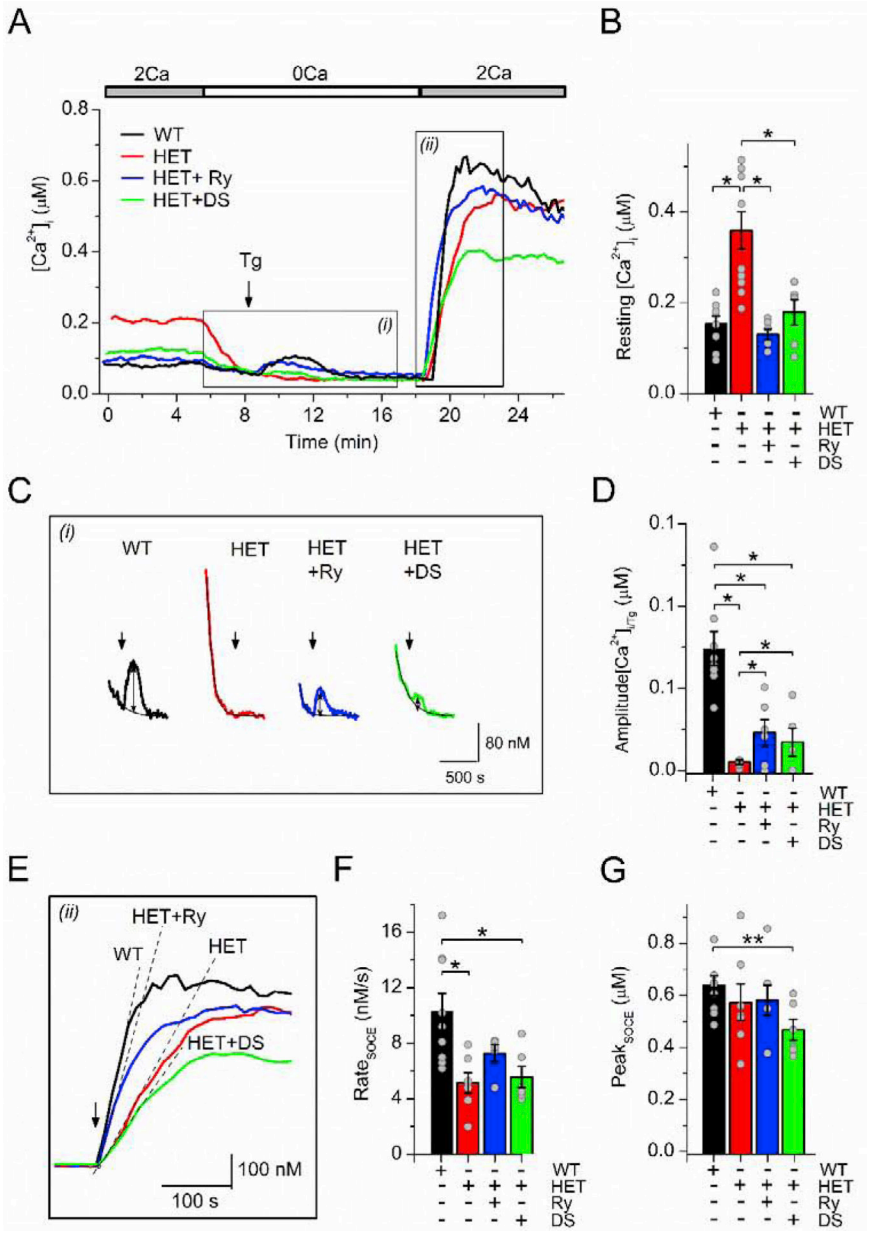

Figure 3. Activated HET T cells display differences in resting $[Ca^{2+}]_i$ and changes in $[Ca^{2+}]_i$ in response to stimulation compared with WT T cells.

A, Changes in $[Ca^{2+}]_i$ recorded from activated WT T cells (black trace), HET T cells (red trace), HET T cells preincubated with 400 μM Ry (blue trace) or 50 μM DS (green trace). Each trace is an average of 12–20 traces recorded from the single cells. Traces are from the representative experiments. 2 mM Ca^{2+}-containing (2Ca) and nominally Ca^{2+}-free (0Ca) solutions were applied as indicated by horizontal bars; the timing of application of Tg (1 μM) is indicated with an arrow.

B, Levels of resting $[Ca^{2+}]_i$ measured as an average $[Ca^{2+}]_i$ within 4 min after the beginning of the experiment in WT T cells (black bar, n = 9; data from 8 mice), HET T cells (red bar, n = 10; data from 8 mice), and HET T cells preincubated with 400 μM Ry (blue bar; n = 6;

data from 4 mice) or 50 μM DS (green bar; n = 6; data from 5 mice). n – the number of experiments.

C, Traces from the boxed area (i) in A on an expanded scale. Smooth curved lines are single exponential fits of the $[Ca^{2+}]_i$ decline in a virtually Ca^{2+}-free solution. The amplitude of the Tg-elicited $[Ca^{2+}]_i$ transient was calculated as the difference between maximal $[Ca^{2+}]_i$ level after Tg application and extrapolated level of $[Ca^{2+}]_i$ decline obtained by an exponential fit (shown with double-sided arrows). Arrows indicate the timing of the Tg application.

D, Amplitudes of Tg-elicited $[Ca^{2+}]_i$ transients in WT T cells (black bar; n = 8; data from 8 mice), HET T cells (red bar; n = 10; data from 8 mice), HET T cells preincubated with 400 μM Ry (blue bar; n = 6; data from 4 mice) or 50 μM DS (green bar, n = 5; data from 5 mice).

E, Traces from the boxed area (ii) in A on an expanded scale. Straight dashed lines show extrapolated linear fits of the initial segment of $[Ca^{2+}]_i$ elevation following Ca^{2+} re-addition. Slopes of these linear functions correspond to the maximum rate of $[Ca^{2+}]_i$ elevation. Arrow indicates the timing of the re-addition of 2 mM Ca^{2+}-containing extracellular solution.

F & G, Maximum rates of $[Ca^{2+}]_i$ elevation following Ca^{2+} re-addition ($Rate_{SOCE}$) and maximal (peak) levels of $[Ca^{2+}]_i$ following Ca^{2+} re-addition ($Peak_{SOCE}$), correspondingly, recorded from WT T cells (black bars; n = 9; data from 8 mice), HET T cells (red bars; n = 7; data from 7 mice), HET T cells preincubated for 30 min with 400 μM Ry (blue bars, n = 5; data from 4 mice), and HET T cells preincubated for 30 min with 50 μM DS (green bars, n = 6; data from 5 mice). In all bar graphs, brackets above bars indicate that differences between group means are significant ($p \leq 0.05$; *false discovery rate ≤ 5%; ** false discovery rate ≤ 10%;). Scattered dots overlaid over bar graphs are measurements from the individual experiments. Each dot is an average of 12–20 measurements from individual cells.

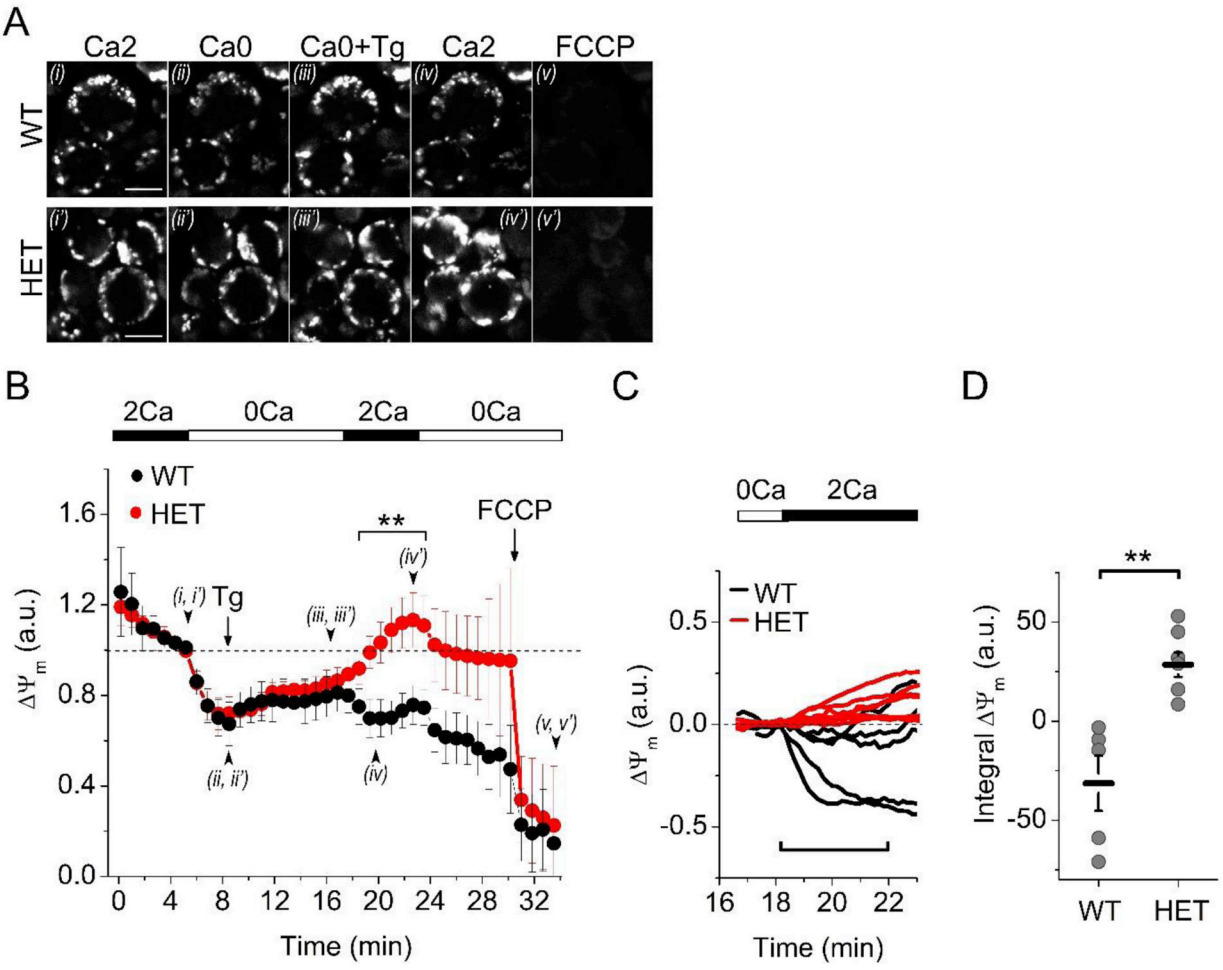

Figure 4. Activated HET and WT T cells display differences in changes in $\Delta\Psi_m$ after SOCE activation.

A, TMRM fluorescence recorded in WT (upper panels) and HET (lower panels) activated T cells in a bath solution containing 2 mM Ca^{2+} (Ca2; panels *i* and *i'*; *iv* and *iv'*), nominally Ca^{2+}-free bath solution (0Ca; panels *ii* and *ii'*), or nominally Ca^{2+}-free bath solutions supplemented with Tg (1μM; Ca0+Tg; panels *iii and iii'*) or FCCP (10 μM; panels *v and v'*). Solutions were applied sequentially as shown in B. Images shown in panels *i* – *v* and *i'* – *v'* were acquired at the times shown in B. Scale bars, 5 μm.

B, Relative changes in $\Delta\Psi_m$ recorded from activated WT (black trace) and HET (red trace) T cells expressed in arbitrary units of TMRM fluorescence intensity. A mean TMRM fluorescence was measured in the regions of interest outlining the puncta. A decline in $\Delta\Psi_m$ indicates a more depolarized $\Delta\Psi_m$. Each point is an average and ± SE of measurements obtained in 5 and 6 experiments performed using WT and HET T cells, respectively. 2 mM Ca^{2+}-containing (2Ca) and nominally Ca^{2+}-free (0Ca) solutions were applied as indicated by horizontal bars; timing of application of Tg (1 μM) and FCCP is indicated with arrows. Arrowheads and numbers *i* – *v* and *i'* – *v'* indicate times at which corresponding images shown in A were acquired. Bracket and asterisks (**) indicate the region where differences between means are significant ($p < 0.01$; independent Student *t*-test). Before averaging, the value of TMRM fluorescence recorded 30 min after FCCP application was taken as

background and subtracted from the raw TMRM fluorescence intensities. Immediately before the application of a nominally Ca^{2+}-free solution, TMRM fluorescence values were normalized to 1 in each experiment (dashed line). Each trace obtained from an independent experiment is an average of fluorescence intensity traces obtained from 10–20 individual cells. Data were obtained using T cells isolated from 3 WT and 3 R163C HET mice.

C, Expanded area indicated with a bracket in ***A*** showing changes in normalized $\Delta\Psi_m$ in response to Ca^{2+} re-addition, recorded from activated WT (black traces) and HET (red traces) T cells in individual experiments. Traces were normalized as described in ***A*** and aligned at the time of the Ca^{2+} re-addition; $\Delta\Psi_m$ level at the time of the Ca^{2+} re-addition was set to 0 (dashed line). Bracket indicates a 4-min interval for which integration of $\Delta\Psi_m$ traces was performed. Each trace is an average of TMRM fluorescence intensities measured in 10–20 individual cells in a single experiment.

D, Average ± SE (horizontal bars) and individual experiment (circles) values of the integrals of changes in $\Delta\Psi_m$ during the first 4 minutes after re-addition of extracellular Ca^{2+} obtained from HET and WT T cells. Asterisks (**) indicate that differences between means are significant ($p < 0.01$; independent Student *t* test).

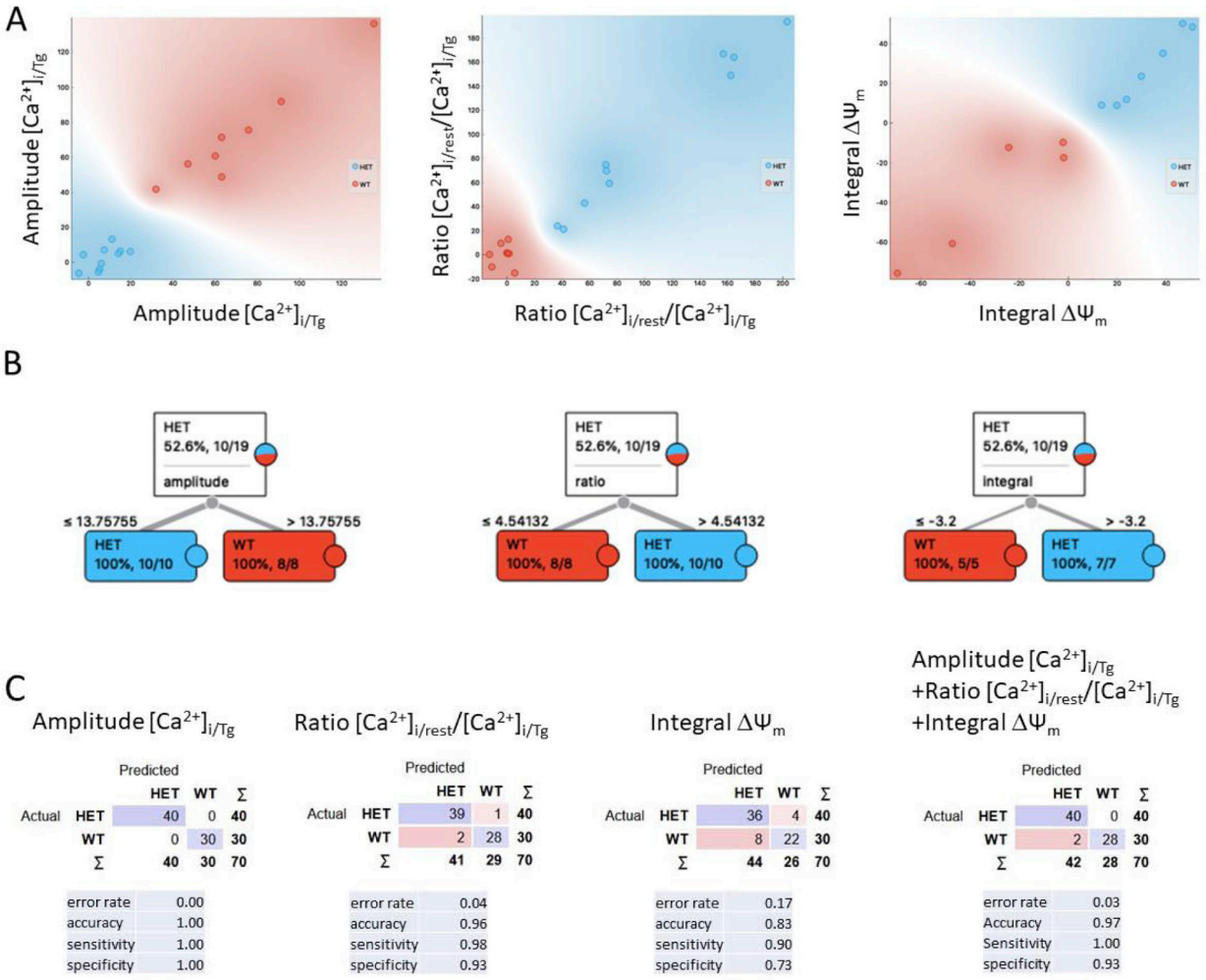

Figure 5. Separation of populations of HET and WT T cells using statistical learning analyses.

A, Classification decision boundaries obtained using exploratory Classification Tree workflow learning algorithm in Orange3 software and the amplitude of the Tg-evoked $[Ca^{2+}]_i$ transients (Amplitude$[Ca^{2+}]_{i/Tg}$; data from Fig. 3D), the ratio of resting $[Ca^{2+}]_i$ to the amplitude of the Tg-evoked $[Ca^{2+}]_i$ transients (Ratio$[Ca^{2+}]_{i/rest}/[Ca^{2+}]_{i/Tg}$; data from Fig. 3E) or integral of changes in $\Delta\Psi_m$ during the first 4 minutes after re-addition of extracellular Ca^{2+} (Integral $\Delta\Psi_m$; data from Fig. 4C) as single-label classification variables. The blue areas correspond to the class density plot of the HET group (blue dots) while the pink area depicts the class density plot of the WT group (red dots).

B, Classification trees built using a learning algorithm optimizing class differences show that the HET and WT T cells can be classified correctly with 100% accuracy using Amplitude$[Ca^{2+}]_{i/Tg}$, Ratio$[Ca^{2+}]_{i/rest}/[Ca^{2+}]_{i/Tg}$ and Integral $\Delta\Psi_m$ as single-label classification variables. For classification tree building, the following settings were used (Logistic regression Ridge2 rasterization c=1).

C, The confusion matrix calculated using the Cross-Validation workflow in Orange3 software with 10-fold stratified cross-validation; the sampling method settings were logistic regression, random sampling, training set size 66%, repeat train/test 10 times. In a two-step

procedure, a learning algorithm was fitted on a set of training data constituting 66% of data randomly selected from a total data set variable and then evaluated on the remaining test data set. The best predictive outcome was obtained when Amplitude$[Ca^{2+}]_{i/Tg}$ alone was used as a single-label classification variable (the error rate [0%], accuracy [100%], sensitivity [100%], and specificity [100%]).When all three single-label classification variables (Amplitude$[Ca^{2+}]_{i/Tg}$, Ratio$[Ca^{2+}]_{i/rest/}[Ca^{2+}]_{i/Tg}$ and Integral $\Delta\Psi_m$) were used, the error rate (3%), accuracy (97%), sensitivity (100%) and specificity (93%) were calculated from the confusion matrix.